Swiss Accelerator Research and Technology

CHART Scientific Report

FCC-ee High-Temperature-Superconducting Short Straight Section

(FCCee HTS4)

PSI:
Michael Koratzinos, Bernhard Auchmann, André Brem, Matteo Crescenti, Micha! Duda, Jaap Kosse, Kirtana Puthran, Jürgen Schmidt

CERN:
Francesco Bardi, Ioannis Dimoulios

29.04.2026

Technical Report: HTS4 Cos-Theta Demonstrator

CONTENTS

I Introduction 1

II Design 2
- II-A Requirements 2
- II-B Electromagnetic Design 3

III Mechanical Assembly 6
- III-A Coil Configuration 6
- III-B Assembly Configuration 6

IV Manufacturing 6
- IV-A Coating Process 6
- IV-B Coil Winding 6
- IV-C Curing Process 7
- IV-D Splice Connections, Current Leads and Instrumentation 9
- IV-E Vacuum Impregnation 9

V Test Results 10
- V-A Instrumentation and Test Setup 10
- V-B Electrical Performance at 40 K 10
- V-C Critical Current Performance 13

VI Conclusions 13

I. INTRODUCTION

The baseline FCC-ee main storage ring magnet configuration consists chiefly of iron-dominated normal conducting dipoles, quadrupoles and sextupoles [1]. The latter two form the short straight sections and consume a large amount of power (up to 79 MW [2]). By replacing the normal-conducting quadrupoles and sextupoles by HTS-based systems, several benefits can be obtained: significant power savings (from 79 MW down to 12 MW), an increase in dipole filling-factor, and flexibility in the optics design [3]. The power savings result from a reduction in dissipation in the magnets as well as from a reduction in synchrotron radiation due to the increased dipole filling factor (which increases the effective bending radius). Demonstrating the advantages and feasibility of HTS-based short straight sections (SSS) is the goal of the CHART project HTS4. A cross-section of such a fully-nested short straight section is shown in Figure 1.

Key to the energy-efficient operation of the HTS magnet system is the operation at relatively high temperatures (around 40 K), required to keep the power consumption of the cryogenic system low. The optimum operating conditions follow from balancing operational costs with capital expenditure. Elements to the solution are: magnets with efficient conductor use and low component cost, a cost-effective, operationally efficient and highly reliable cryogenic system [4], a powering concept that minimizes heat input at the leads [5] while ensuring high system availability, and a beam dynamics concept that takes full advantage of the new coil arrangement.

This work was performed under the auspices of and with support from the Swiss Accelerator Research and Technology (CHART) program (www.chart.ch)

As part of the HTS4 initiative, a demonstrator sextupole magnet of a cosine-theta configuration, designated *Ozzy*, has been designed, constructed, and tested. The cosine-theta geometry refers to a winding pattern where the current-density in the cross-section follows a (co)sinusoidal distribution around the magnet bore, providing optimal magnetic field shaping for multi-pole magnets while maximizing conductor utilization efficiency. This demonstrator represents a proof-of-concept for the feasibility of HTS magnet technology in high-energy physics applications, addressing key technical challenges including coil manufacturing, cryogenic operation, and electrical performance under realistic operating conditions. Field quality will be addressed in the next stage of the project, where a longer nested sextupole/quadrupole magnet will be delivered for a full evaluation of FCC-ee design specifications.

The REBCO demonstrator uses a 4 mm tape with self-bonding coating technology, allowing for post-winding coil curing, and providing a controlled turn-to-turn resistivity. The resistivity value is tuned to reproduce steel-tape metal insulation [6], which has been proven to provide intrinsic quench protection for magnets of a similar class. The magnet was designed for operation at 40 K with current-carrying capacity up to 370 A. It features comprehensive instrumentation for voltage measurement across individual coils and splice joints, alongside Hall sensor arrays in the magnet bore for first-order magnetic field characterization.

This report presents the complete development and testing of the HTS4 cos-theta demonstrator magnet conducted in 2025, encompassing design, manufacturing, and electrical characterization from 30 K to 70 K. Section II details the requirements and electromagnetic design of the demonstrator. Section III describes the coil configuration and magnet assembly. Section IV describes the partial insulation coating processes, automated winding technique, thermal curing procedure, splice connections, and vacuum impregnation used in magnet construction. Section V presents the experimental results including instrumentation setup, electrical performance characterization under nominal operating conditions of 40 K, temperature-dependent critical current measurements and analysis of electromagnetic decay time. Section VI summarizes the development and test results of the demonstrator and provides perspectives for future work in the project.

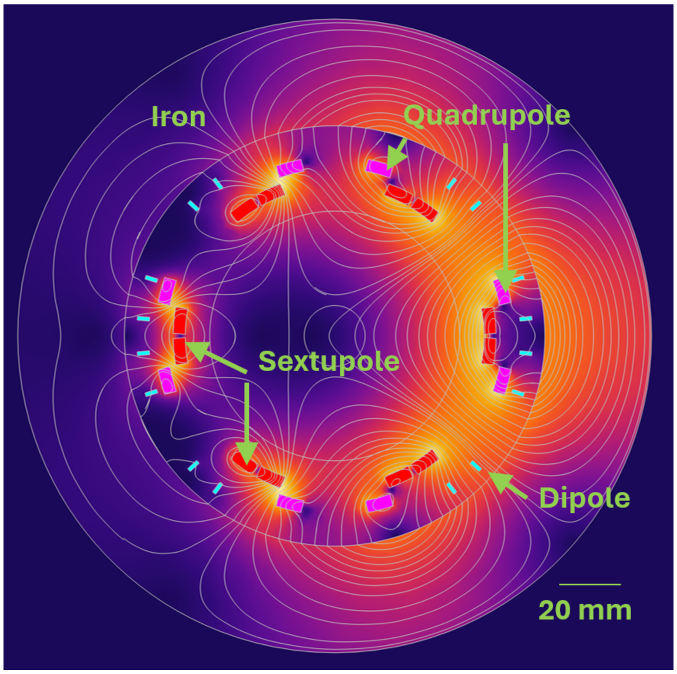

Fig. 1: Example of a cross-section of fully-nested HTS short straight section based on a sextupole, quadrupole and dipole, formed by an assembly of cosine-theta coils.

TABLE I: Maximum required integrated strength per harmonic per short section, at a 10 mm reference radius[7]. White-backgrounds indicate requirements, yellow backgrounds indicate derived values or design choices.

Harmonic	$\lvert\int B_n \mathrm{d}z\rvert$ [Tm]	L_{mag} [m]	$\lvert B_n\rvert$ [T]
Dipole (SSS)	0.1459	2.9	0.0503
Quadrupole	0.3439	2.9	0.1186
Sextupole	0.1345	2.7	0.0498
Hor. dip corrector	0.0174	2.9	0.006
Vert. dip corrector	0.0174	TBD	TBD
Skew quadrupole	0.0058	TBD	TBD

II. Design

A. Requirements

The electromagnetic design of the demonstrator sextupole magnet is based on a potential short straight section implementation involving a nested sextupole and quadrupole configuration; eventually also including a nested dipole, which would render the short straight sections curved. Here 'nested' means that the magnets share the same axial space. The short sections formed by these quadrupoles and sextupoles (and ultimately dipoles) form the double-aperture main ring together with normal-conducting dipoles. There would be around 2900 short straight sections. By including nested HTS dipoles with the quadrupole and sextupole, we aim at a 100% dipole filling factor.

Replacing the normal-conducting sextupoles and quadrupoles with HTS variants, and ensuring a high dipole filling factor could be achieved via two implementations. One could either put a nested dipole/quadrupole in sequence with a nested dipole/sextupole or fully nest all three harmonics. The quadrupole cannot be shorter than 2.9 m due to synchrotron radiation considerations[3]. This means that a dipole+quadrupole in series with a dipole+sextupole will result in a longer magnet than a fully nested system. The advantage of such an approach would be that the superposition of field of the different coil sets on each other would be less. For the conceptual study, we chose the fully nested configuration.

Requirements on magnets for a short straight section based on nested magnets and a maximized dipole filling factor are listed in[7]. The magnetic field strength that each harmonic set needs to generate is relatively modest, leading to peak fields on the windings of around 2 T. The magnetic field profile in the bore of a combination of dipole, quadrupole, and sextupole components can be expressed as a strength B_1, B_2, B_3, respectively. This is achieved by performing a Fourier expansion at a certain reference radius[8], in this case 10 mm. The maximum required strengths are defined by the operation in the highest energy mode, $t\bar{t}$[1].

From the integrated strength requirements, listed in Table I, the strengths are derived as follows: the quadrupole minimum magnetic length is fixed by synchrotron radiation limits, and we set the quadrupole length to this minimum (2.9 m). The dipole ideally covers as much length as possible, so it is set to the same length as the quadrupole. The sextupole is set slightly shorter, to 2.7 m, to allow axial space for other correction coils.

The sextupoles in each short straight section need to be able to be independently set and may have a negative or positive polarity. At the moment, there is no expectation that the sextupoles in both beam lines have the same strength or polarity.

A nested dipole belonging to a defocused quadrupole has the same strength requirement as the main dipoles, but a dipole nested with a focused quadrupole only requires 53% of the strength[3], due to higher-order effects of the quadrupole on the beam trajectory. This makes it desirable to have the quadrupoles for both beams within a given short section provide the same function (i.e. either focus or defocus), as that allows both dipoles in one short section to have the same strength and thus be powered by the same power supply.

As a given quadrupole might have a defocusing role in Z-mode, and focusing in $t\bar{t}$-mode, whereas its dipole always generates a positive field, this makes combined function magnets, in which one coil set generates multiple harmonics, unattractive for this particular application.

As we judged that out of the 3 harmonics (B_1/B_2/B_3) the sextupole would be the most difficult magnet from a manufacturing perspective, for a first demonstrator this would be the harmonic to try to build.

There are three main reasons why we propose a cosine-theta geometry for all three coil-sets.

- The cosine-theta, neglecting the possible advantages of field-aligned configurations, is the most conductor-efficient coil type, and it enables efficient nesting of various multi-pole arrangements, similar to the LHC nested corrector magnets.
- A cosine-theta geometry does not need a complex winding mandrel, saving costs.

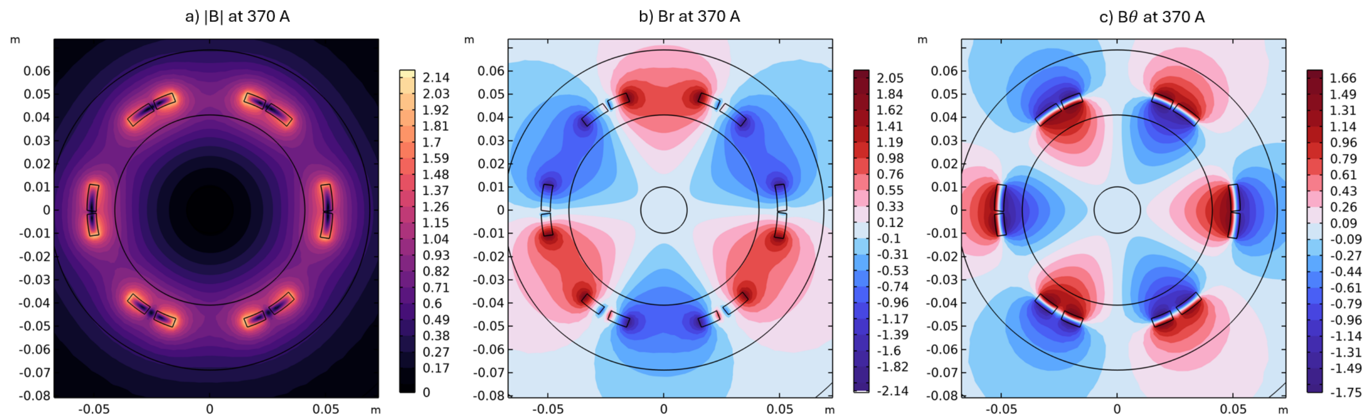

Fig. 2: Sextupole demonstrator magnetic field distribution a) norm, b) radial component, c) azimuthal component, at a current of 370 A.

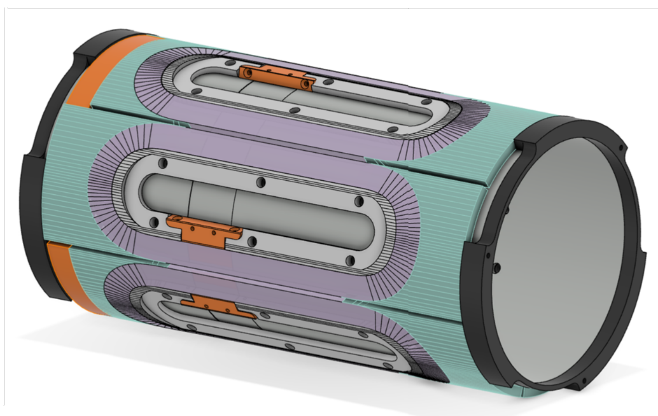

Fig. 3: Individual coils connected in series through inner and outer splices to form the sextupole magnet configuration on the magnet bore.

TABLE II: Comparison of SSS and demonstrator

Parameter	Unit	SSS	Demonstrator
Turns per cross-section (1 aperture)			
Sextupole		492	492
Quadrupole		240	0
Dipole		80	0
Current			
Sextupole	A	320	370
Quadrupole	A	320	0
Dipole	A	67	0
Field at 10 mm reference radius			
B_3	mT	50	50
B_2	mT	120	0
B_1	mT	51	0
Iron yoke		yes	no
Current sharing temperature T_{cs}	K	40	40
Conductor		ReBCO	ReBCO

- The winding of the cosine-theta coils, as will be demonstrated in this report, can be automated.

TABLE III: Parameters of the HTS4 cos-theta demonstrator magnet

Parameter	Value
No. of turns per coil	82
No. of coils	6
Tape length per coil (m)	34
Minimum bending radius (mm)	16
Straight section length (mm)	110
Operating current (A)	370
Sextupole field strength (mT)	49.8
Peak field on conductor (T)	2.2
Inductance (mH/m)	54.8
Maximum torsion (1/m)	67
Maximum normal curvature (1/m)	95
Maximum geodesic curvature (1/m)	16

B. *Electromagnetic Design*

The design choices described below are derived first for the SSS; the demonstrator sextupole inherits them, and departs from the SSS design only where stated. In addition to the goal of generating a sextupole component of 0.0498 T, an additional constraint we placed on the SSS was a current sharing temperature of 40 K. This resulted from an optimization of the operating temperature and adding a temperature margin to that. This optimization, which is not part of this document, balances operational costs (dominated by electricity use required for cooling of the superconductor) and capital costs (dominated by the superconducting tape). An additional result from the optimization is that 4 mm-wide tape is preferred over the other commercially available options (2 mm and 12 mm). Moreover, the space between the beam wall and the sextupole must accommodate 1) a cryostat wall, 2) multi-layer insulation, and 3) an inner mandrel on which the coil is attached, from which a minimum inner sextupole radius of 49 mm is derived.

As a first step towards the sextupole design, the 2D field quality was investigated. The effects of screening currents are not part of this analysis. It was found that one could already achieve decent magnetic field quality (unwanted terms smaller than 1 unit) by using just one conductor block per pole. This could in reality be achieved by 3 coils, whose legs would form the 6 poles of the sextupole. Subdivision of

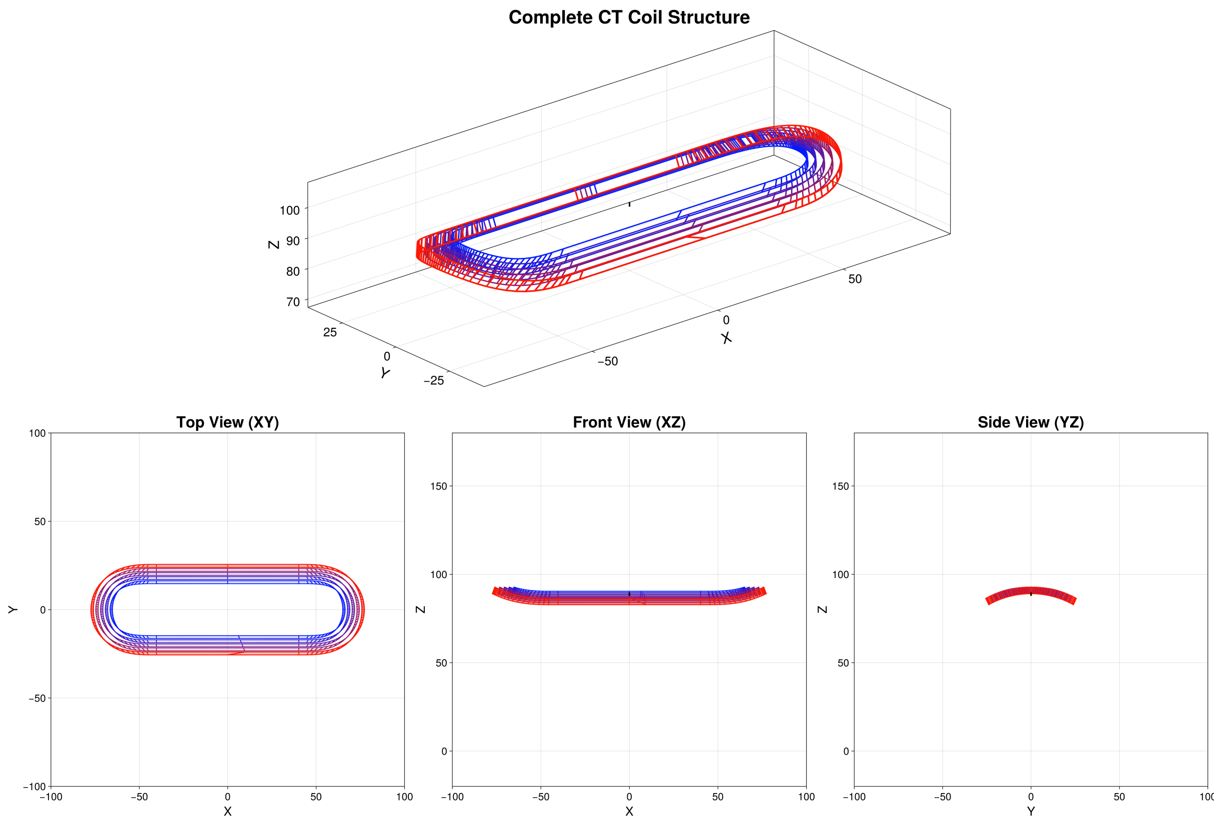

Fig. 4: Cos-theta coil structure geometry showing conductor arrangement with a few individual turns visible in 3D view and orthogonal projections displaying coil dimensions.

the poles is not required to meet the magnetic field quality targets. This follows from the small relative ratio of the harmonic reference radius (10 mm) to the sextupole inner radius (49 mm). The choice was made to subdivide each pole into 2 blocks (Figure 1), as this would result in a 6-coil sextupole, with the advantage that the hard-way bending in the coil-end would be smaller than for a 3-coil configuration. The quadrupole poles were split into two blocks per pole, realizable with 4 coils (Figure 1). The dipole on the other hand was found to require more subdivision, with 4 blocks per pole yielding good field quality.

The demonstrator reproduces the sextupole of the SSS only. Whereas a full-scale SSS would feature two apertures, and iron shielding to reduce the cross-talk between different apertures' magnets, it was decided to omit iron for the sub-scale demonstrator. The two designs are compared in Table II: the cross-section is identical at 492 turns, but without the iron yoke the demonstrator requires 370 A rather than 320 A to reach the same sextupole field of 50 mT at 10 mm. As a side note, when the project started, an operating temperature of 40 K, an operating current of 250 A and a targeted sextupole field of 40 mT was foreseen. The two sets of specifications are compatible, i.e., the demonstrator would meet these specs if an iron yoke were introduced.

The REBCO tape used in the demonstrator is produced by Faraday Factory Japan. The tape width is 4 mm, Hastelloy thickness $38\,\mu\mathrm{m}$, copper thickness $20\,\mu\mathrm{m}$/side. The two spools used have an average critical current, I_c (77 K, S.F.) of 237.1 A and 235.2 A, with standard deviation 4.9 A and 3.35 A. To estimate the expected performance of the sextupole, a scaling law of the form proposed by[9] is used. The $I_\mathrm{c}(B,T,\theta)$ behavior of the tape is taken from[10,11] and represents SuperOx YBCO tape[1]. A scaling factor is used to match the 77 K self-field performance of the actual tape, as measured by the manufacturer.

The two-dimensional electromagnetic design was carried out in COMSOL without an iron yoke, while ROXIE was used to generate the three-dimensional coil-end geometry, by optimising the coil-ends to reduce the hard-way bending as much as possible. The computed field distribution of the demonstrator at 370 A is shown in Figure 2. The peak field on the conductor is 2.2 T. The two-dimensional inductance of the sextupole cross-section is 54.8 mH/m, giving 6.0 mH over the 110 mm straight section, with a further contribution from the two coil ends. For protection, the magnet relies on turn-to-turn current sharing through the partial insulation. A turn-to-turn contact resistance of 100 mΩ·cm^2 was set as the target for the coating (Section IV-A), selected from the range reported in the literature for metal-as-insulation REBCO coils[6]. For a coil of 82 turns with an average turn length of 415 mm and a tape width of 4 mm, each turn-to-turn interface has an area of 16.6 cm^2, giving a radial resistance of 0.49 Ω per coil, and 3.0 Ω for the six coils of the magnet. Taken with

[1]Tape with similar performance is obtainable from Faraday Factory Japan.

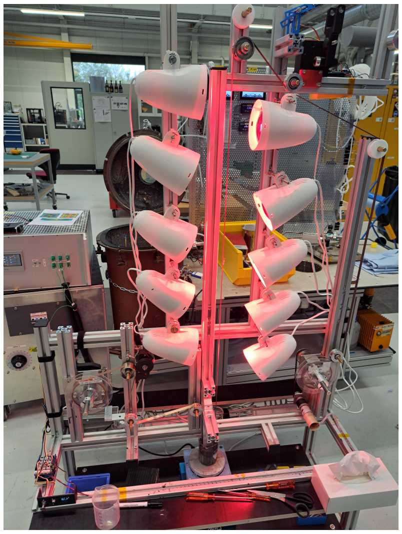

(a) Dip-coating process setup showing continuous tape processing through PVB solution bath with infrared drying section.

(b) Image of PVB-coated HTS tape showing the uncoated edges.

Fig. 5: Novel partial insulation developed in order to tune the quench characteristics of the coils.

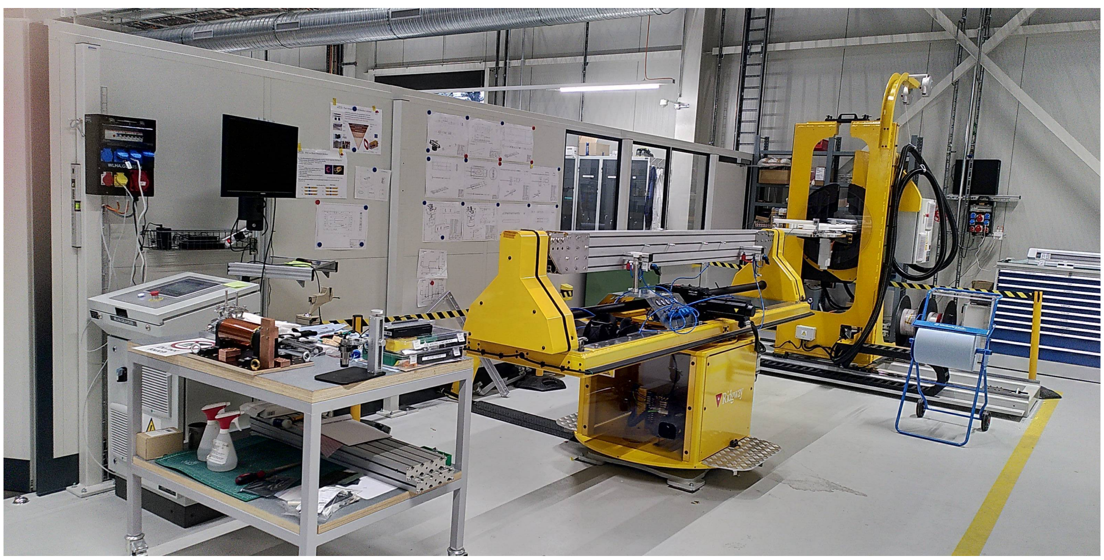

Fig. 6: 5-axis winding machine used for automated cos-theta coil fabrication, showing the coordinated control system for V-axis (vertical rotation), H-axis (horizontal rotation), X-axis (longitudinal positioning), Z-axis (vertical positioning), and R-axis (tape rotation).

the corresponding inductance this gives a characteristic decay time $\tau = L/R_{\perp}$ of about 2 ms.

The turn-to-turn resistance of the coils is aimed to be in the same range as metal-insulated coils [6], but relies on a self-bonding coating layer instead of on contact pressure between turns. The inspiration for our coating comes from the wire industry [12]. There, the metal wire is covered first by the actual electrical insulation layer, on top of which the bonding layer is applied. Winding packs wound from this type of wire can be fused into a solid piece by either solvent-based or heat-based bonding. Our idea is to skip the typical insulation layer, and to achieve a desired contact resistance by applying a conductive bonding layer directly around the conductor.

If instead the coil would be wound from insulated tape, protected by external discharge over a dump resistor, the copper thickness of $20\,\mu\text{m}$/side would not have been sufficient to prevent excessive temperatures, if a quench would occur at 370 A. The inclusion of additional copper, as well as the insulation thickness itself ($15\,\mu\text{m}$/side) would result in thicker turns, and thus in more of the turns being placed in less-effective areas, leading to a higher required number of turns per coil. As an example, a set of 6 coils at 320 A based on $100\,\mu\text{m}$ thick turns would need 78 turns per coil, whereas with $140\,\mu\text{m}$ thick turns, 85 are needed.

The key design parameters for the HTS4 cos-theta demonstrator magnet are summarized in Table III.

III. Mechanical Assembly

This section describes the mechanical aspects of the coil configuration and the structural elements that form the complete magnet assembly.

A. Coil Configuration

The magnet features six individual coils arranged in cos-theta geometry and positioned concentrically around a central bore with an outer diameter of 98 mm. Figure 3 shows the coil configuration on the central bore. The six coils are positioned on this bore using placement pins to ensure accurate angular and radial alignment.

Each coil has 82 turns, 110 mm straight sections and a minimum bending radius of 16 mm. Figure 4 illustrates the three-dimensional coil geometry with orthogonal projections showing dimensional details. The coils are connected in series. Two types of electrical connections link the coils: outer splices connect via the outermost turn, whereas inner splices use the first turn, through copper blocks and 12 mm HTS tape segments. The interconnections comprise three inner and two outer splices.

B. Assembly Configuration

The inner stainless steel bore with the assembled coils is inserted into an aluminum alloy shell. The shell provides the primary structural containment for the coil assembly. Aluminum was chosen as a compromise between costs and thermal conductivity. Once positioned within the shell, the coil assembly undergoes vacuum impregnation with alumina-filled wax. The wax provides thermal conduction pathways and distributes mechanical loads uniformly across the assembly.

The current leads of the magnet extend from the terminals of the two end coils through dedicated feed-through points in the shell wall. These leads provide electrical connection to the external circuit while minimizing thermal conduction. The voltage tap instrumentation feed-through ports (not shown in the figure) enable individual coil and splice joint monitoring during electrical characterization. The copper connection blocks mounted on top of the exterior aluminum shell are a mechanical and thermal interface with the cryostat system, and carry mounting points for heaters. Electrical isolation is maintained using thermally conductive insulating epoxy.

IV. Manufacturing

The manufacturing process of the magnet follows a sequential five-stage approach comprising 1) coating of the HTS tape, 2) winding of the coils, 3) thermal curing of the partial insulation, 4) introduction of inter-coil electrical connections or splices, current leads and instrumentation, and 5) vacuum impregnation.

A. Coating Process

The coating process employs a continuous dip-coating methodology[13] utilizing polyvinyl butyral (PVB) as the thermoplastic matrix with graphite powder as conductive fillers. The coating composition consists of 30 v% 5 μm graphite powder in low molecular weight PVB dissolved in acetone solvent at 12.5 v% concentration, providing controlled viscosity for uniform layer deposition. The coating formulation, developed for the HTS4 project, targets turn-to-turn contact resistance values above 100 mΩ·cm^2 while maintaining processing characteristics favorable for large-scale coil manufacturing applications. Figure 5a shows the dip-coating process setup, and an image of the coated HTS tape is shown in Figure 5b. The coating process employs continuous stirring of the bath solution to maintain homogeneous filler dispersion and infrared heating for solvent evaporation, currently achieving coating thicknesses of 5–20 μm. Due to the characteristic cross-sectional geometry of the HTS tape, the coating does not cover the tape edges. This effect does not seem detrimental to the coil performance.

B. Coil Winding

The winding process is carried out on a 5-axis winding machine shown in Figure 6 with coordinated control of vertical rotation (V-axis), horizontal rotation (H-axis) of the beam, as well as longitudinal (X-axis), vertical positioning (Z-axis), and tape rotation (R-axis) of the pay-off. The winding process represents a control problem due to the non-planar coil geometry. It requires simultaneous coordination of five machine axes to maintain optimal tape contact and alignment at each winding position.

A program has been written in the Julia programming language to address the winding problem. The algorithm of the program transforms the coil surface geometry into machine-readable coordinates through systematic coordinate transformations and optimization calculations. Considering an angular rotation of the winding beam (typically 42 steps per 360°), the algorithm identifies the target surface element with maximum radial extent after V-axis rotation, then calculates the corresponding H-axis angle required to align the surface tangent with the horizontal plane for optimal tape contact. The payoff head position is calculated from the surface normal vector projection to ensure the tape width aligns perpendicular to the surface curvature, preventing tape edge lifting during application. A visual representation of this calculation is shown in Figure 7. The program also accounts for the varying coil radius and surface orientation throughout the winding process. The resulting sequence data includes all five machine coordinates (V, H, X, Z, R) along with process parameters such as winding speed and tension values, formatted as CSV output compatible with the control system of the winding machine.

The automation system successfully generates complete winding sequences for the cos-theta geometry, eliminating manual winding and ensuring consistent tape placement across all the turns of each coil.

During the winding operation, the initial 25–30 turns of a coil are completed without additional tooling support. After this, anodized aluminum clamping fixtures, shown in Figure 8, are installed to provide lateral support as the coil diameter increases with successive winding layers. The clamping fixtures require incremental repositioning to accommodate the growing coil geometry while maintaining the continuous winding process. The coils are wound with a maximum tension of 35 N

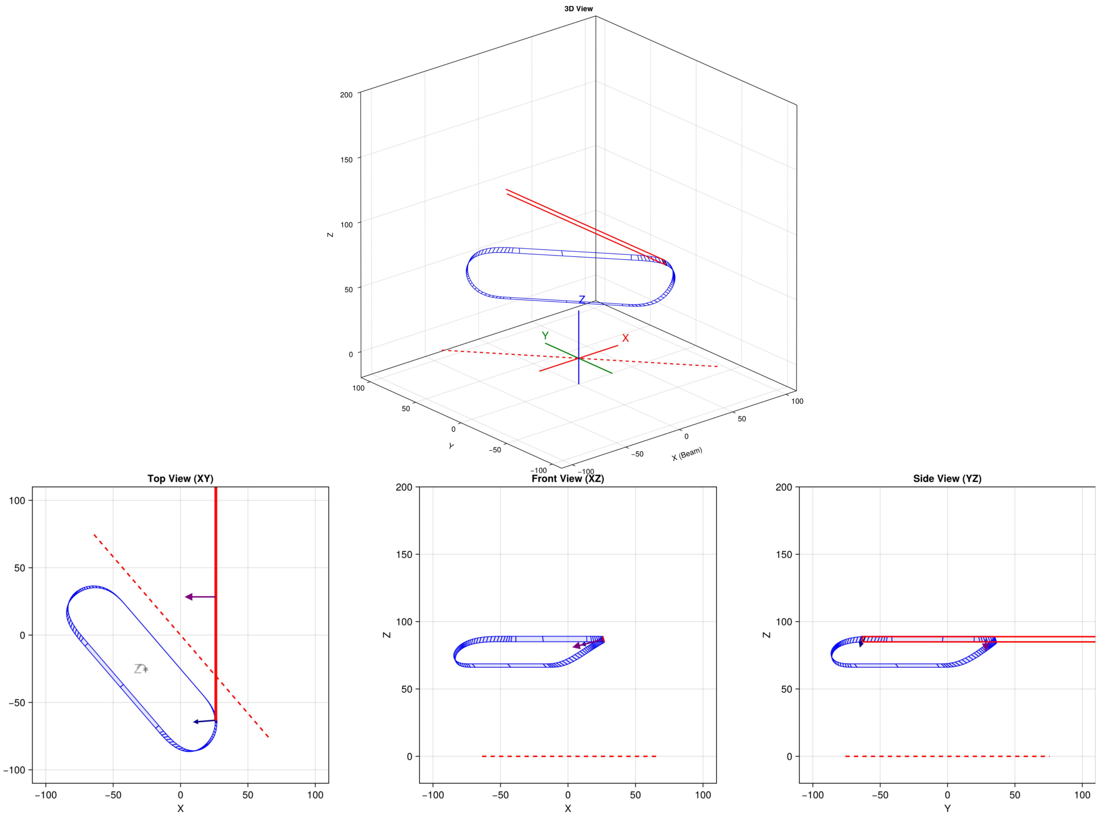

Fig. 7: Example winding position showing the coordination of all five machine axes in the global coordinate axes. The projections illustrate how the three-dimensional surface geometry is mapped to specific machine coordinates for this winding step.

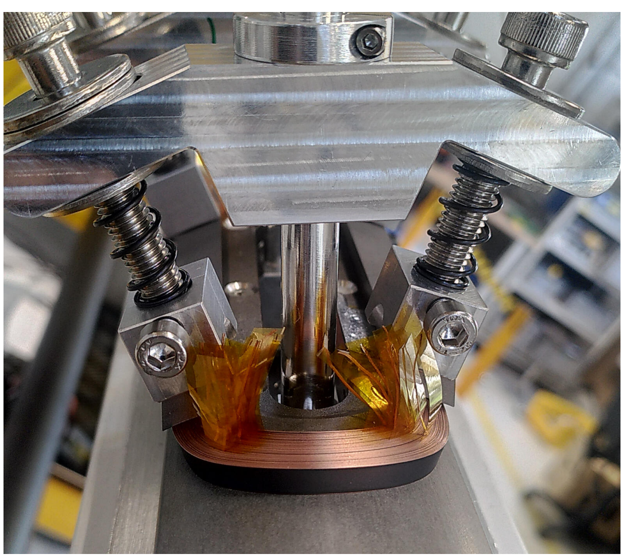

Fig. 8: Anodized aluminum clamping fixtures providing lateral support during cos-theta coil winding. The tooling is incrementally repositioned to accommodate growing coil diameter while maintaining automated winding capability throughout the 82-turn process.

on the tape. During the manufacturing of one coil, C4, the tape was damaged by accidental contact with a scalpel, shown in Figure 11. The coil was retained in the magnet assembly, and the consequences for its performance are reported in Section V-B.

C. Curing Process

Upon completion of winding, additional anodized aluminum tooling is used to hold the coil assembly from the sides for the thermal curing operation of the coating. The curing process involves a controlled thermal treatment up to 175°C, which fuses the coating from adjacent turns together, yielding a monolithic winding pack. The heat treatment duration and temperature are based on target contact resistance specifications. All tooling components feature anodized surfaces in order to provide electrical isolation of the coils. This enables *in-situ* measurement of coil resistance throughout the curing and ensures reproducibility of the turn-turn contact resistance of different coils. Figure 9a shows the assembly configuration of the coil for the curing process. The resulting monolithic coil pack is seen in Figure 9b.

Figure 10 demonstrates the evolution of temperature and coil-resistance with time during a representative curing cycle. The coil resistance peaks during the heating phase due to increased electrical resistivity at elevated temperatures, then decreases as the coating fuses and temperature drops.

The turn-to-turn contact resistance represents a critical parameter in partially insulated HTS coils, as it determines the current redistribution characteristics and electromagnetic

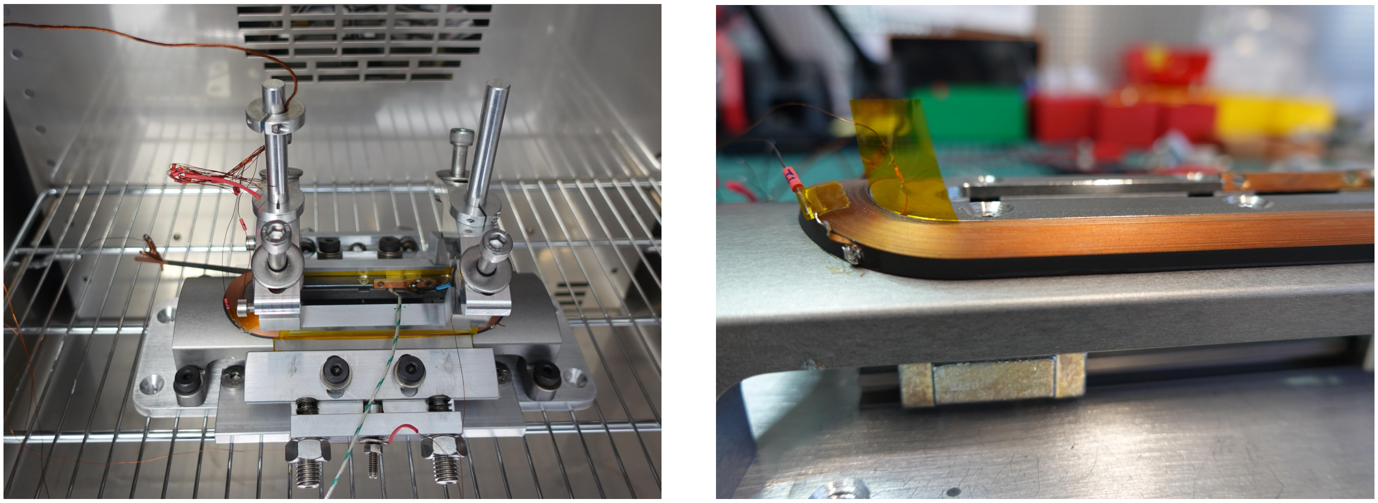

(a) Coil assembly positioned within the curing furnace in preparation for the thermal treatment.

(b) Self-supporting cos-theta coil following thermal curing and tooling removal.

Fig. 9: Thermal curing process of the coating creates mechanically self-supporting coil structures that maintain precise cos-theta coil geometry.

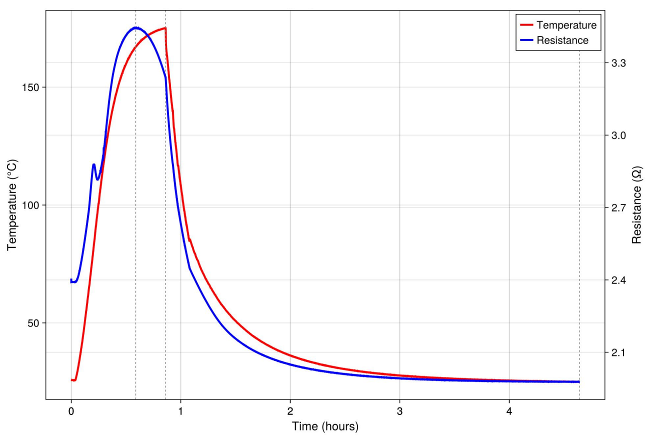

Fig. 10: Temperature and coil resistance monitoring during partial insulation curing, showing resistance development as a function of thermal treatment parameters.

decay behavior. The contact resistance between adjacent turns can be extracted from total coil resistance measurements through circuit analysis.

For a coil with N turns, the total measured resistance R_{coil} comprises two main components: the intrinsic tape resistance R_{tape} and the turn-to-turn contact resistance network $R_{\perp}$. These components are connected in a parallel configuration, where the tape provides a primary current path and the turn-to-turn contacts provide secondary current redistribution paths. The relationship between these resistances is given by:

$$R_{\perp}^{-1} = R_{\text{coil}}^{-1} - R_{\text{tape}}^{-1} \tag{1}$$

At room temperature the tape resistance is dominated by the copper stabiliser. For 40 μm of copper across the 4 mm tape width, a resistivity of 1.71×10^{-8} Ω·m gives $R_{\text{tape}} = 3.6$ Ω over the 34 m of conductor in a coil.

TABLE IV: Individual coil and contact resistances at room temperature following partial insulation curing

Coil	**Max Temperature (°C)**	**Coil Resistance**		**Turn-Turn Resistance (mΩ·cm^2)**
		Max Temp* (Ω)	**25°C (Ω)**	
C1 - Bheema	175	3.24	1.98	901
C2 - Apu	175	3.27	2.12	1056
C3 - Kiwi	180	3.25	2.02	942
C4 - Wasabi	177	3.25	2.17	1119
C5 - Mochi	175	3.26	2.12	1056
C6 - Cookie	178	3.25	2.11	1044

*Coil resistance measured when heating of the coil/furnace is shut down.

The turn-to-turn resistance network $R_{\perp}$ consists of the $N-1$ individual contact resistances between adjacent turns, connected in series. Assuming uniform contact properties, the average turn-to-turn contact resistance per unit area $\bar{R}_{\text{turnturn}}$ can be calculated as:

$$\bar{R}_{\text{turnturn}} = \frac{R_{\perp} \cdot w_{\text{tape}} \cdot \bar{L}_{\text{turn}}}{N-1} \tag{2}$$

where:

- w_{tape} is the tape width
- $\bar{L}_{\text{turn}} = L_{\text{tot}}/N$ is the average turn length
- L_{tot} is the total conductor length per coil
- N is the number of turns per coil

The final coil and contact resistances for each of the six coils used in the demonstrator magnet measured at room temperature are summarized in Table IV, providing baseline electrical characteristics following the curing process.

The primary objective during this phase of the project was to develop and demonstrate a process for controlling contact resistance during curing, addressing the challenge of varying tape surface finish over meter-length scales. Fundamental work on the development of the coating[13] on single tapes

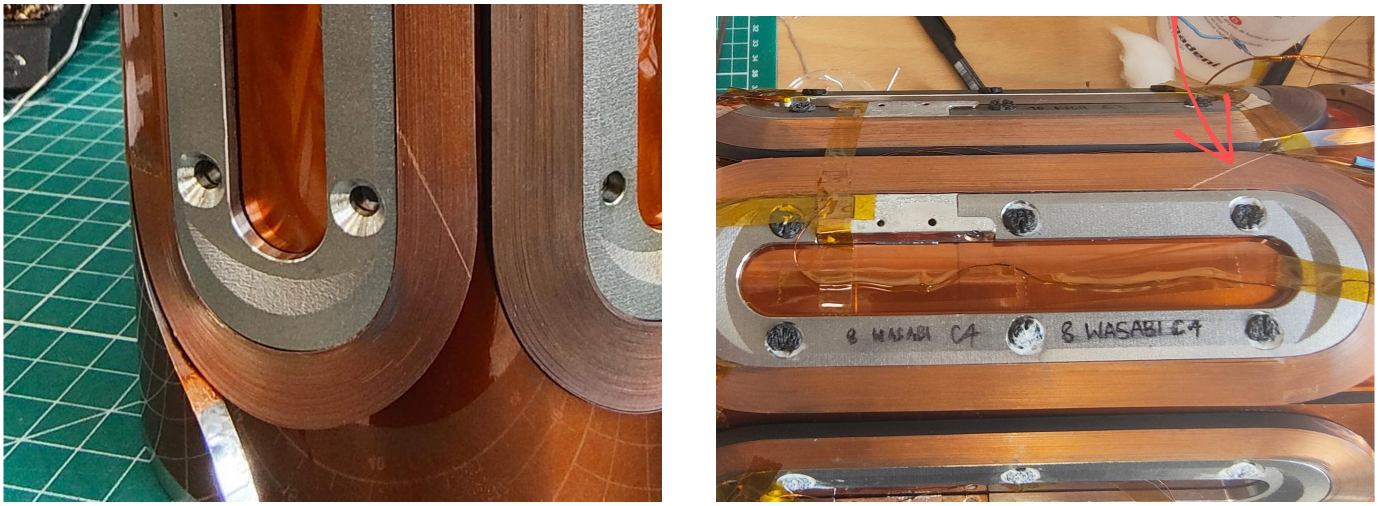

Fig. 11: Physical damage observed in the Coil 4 HTS tape, caused by accidental scalpel contact during manufacturing. Its effect on the electrical performance of the magnet is discussed in Section V-B.

shows the contact resistance at 77 K to be a factor of 2.5–3 lower than at room temperature. The six coils achieved room temperature coil resistances of $2.09 \pm 0.07\ \Omega$ and turn-turn contact resistances of 1020 ± 81 mΩ·cm^2.

During the development phase of the partial insulation methodology, four prototype coils not incorporated into the final magnet assembly were subjected to qualification testing. These development coils underwent multiple thermal cycling sequences between room temperature and liquid nitrogen temperature (77 K) with no observable performance degradation or structural deterioration arising from the curing process. The details of these tests will be provided elsewhere. These measurements confirm the long-term stability and reliability of the PVB-based partial insulation approach for HTS cos-theta magnet applications.

D. Splice Connections, Current Leads and Instrumentation

Prior to vacuum impregnation, electrical connections between coils are established through splices using 60/40 Sn-Pb solder. One each of the three *inner* and two *outer* splices can be seen in Figure 12. The current lead assembly, shown in Figure 13a, provides the electrical interface between the magnet and external power supply. Each current lead consists of a 4 mm HTS tape section soldered in parallel to the outermost turn of the terminal coils, in addition to two pre-soldered copper tape segments of the same width. Mechanical reinforcement is provided by 4 mm wide fiberglass supports integrated into the lead structure.

Each coil is also instrumented with voltage taps at the first and last turn, as seen in Figure 12. This allows for the electrical characterization of all the coils and splices. The instrumentation wires are protected with glass fiber and passed through dedicated feed-throughs in the magnet shell. The coil assembly is covered with a protective polyimide sheet, as shown in Figure 13b, in preparation for the next operation. This ensures electrical insulation of the coils, voltage taps and splices from the external shell.

Fig. 12: View of coil showing inner and outer splice connections and voltage tap locations. Inner splices (IS) are fabricated using 12 mm HTS tape segments, while outer splices (OS) connect the coils via the outermost turns. Voltage taps enable individual coil and splice resistance monitoring during testing.

E. Vacuum Impregnation

Vacuum impregnation with alumina-filled wax represents a novel approach to achieving thermo-mechanical stability in the HTS cos-theta magnets. Following coil winding and instrumentation, the assembled magnet undergoes the impregnation process. Prior to implementing the final procedure, a preliminary test was conducted on a dummy assembly using unfilled wax to validate the impregnation methodology and identify potential process challenges. This trial confirmed void-free filling of the assembly. Impregnation in vacuum eliminates air pockets and enables uniform distribution of the wax throughout the coil geometry, creating a rigid composite structure essential for maintaining dimensional stability during thermal cycling and electromagnetic loading. An image of the magnet assembly post-impregnation is shown in Figure 14.

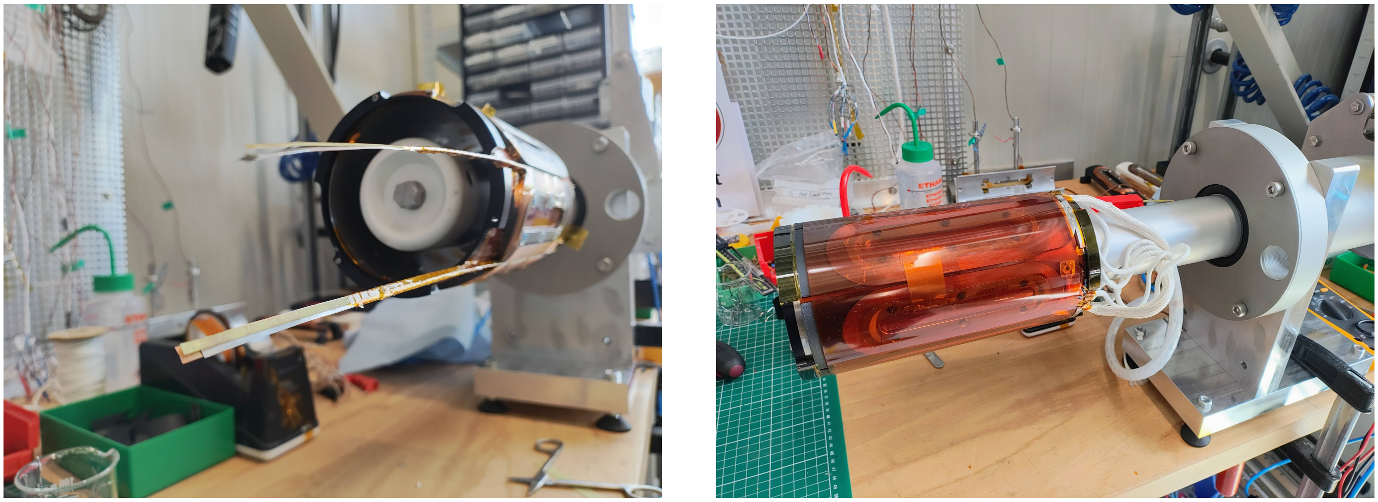

(a) Current lead assembly showing the hybrid HTS-copper conductor configuration with fiberglass mechanical reinforcement.

(b) Magnet assembly prepared for shell insertion showing a polyimide sheet for electrical isolation and instrumentation cables.

Fig. 13: Current lead assembly and magnet assembly preparation showing the hybrid HTS-copper conductor configuration and assembly prepared for shell insertion with protective polyimide covering for electrical isolation.

Fig. 14: Completed vacuum impregnation showing the assembly fully infiltrated with alumina-filled wax.

The extra wax at the top end of the assembly is cleaned for the final configuration.

V. Test Results

This section presents the experimental characterization of the HTS4 cos-theta demonstrator magnet, *Ozzy*. The testing program encompasses electrical performance evaluation at nominal operating conditions, and across the 30–70 K temperature range. Preliminary tests in liquid nitrogen at 77 K are reported elsewhere.

A. Instrumentation and Test Setup

The magnet assembly, mounted within a vacuum cryostat, is shown in Figure 16a. The coil hangs directly under the second stage of a Sumitomo RDK415D GM cryocooler, whose first stage is connected to the thermal radiation shield. A second, single-stage 500B cryocooler cools the metal current leads that transfer the current between room temperature and ∼50 K. The measurement setup included voltage tap monitoring across individual coils and inter-coil splice joints, current monitoring via a DC current transducer on the cables between the power supply and the cryostat, and magnetic field measurements using Hall sensors positioned within the magnet bore. A schematic of the instrumentation comprising the voltage pickups on the coils within the magnet itself is shown in Figure 15, with Hall sensor array positioning shown in Figure 16b. The test methodology follows a three-phase characterization approach:

- **Phase 1**: Minimal characterization at 15 K to verify superconducting state
- **Phase 2**: Full characterization at 40 K nominal operating conditions
- **Phase 3**: Temperature sweep performance mapping (30–70 K)

The following sections present results from Phase 2 (40 K nominal operation) and Phase 3 (temperature sweep).

B. Electrical Performance at 40 K

The electrical characterization at 40 K represents the nominal operating condition for the HTS4 demonstrator magnet.

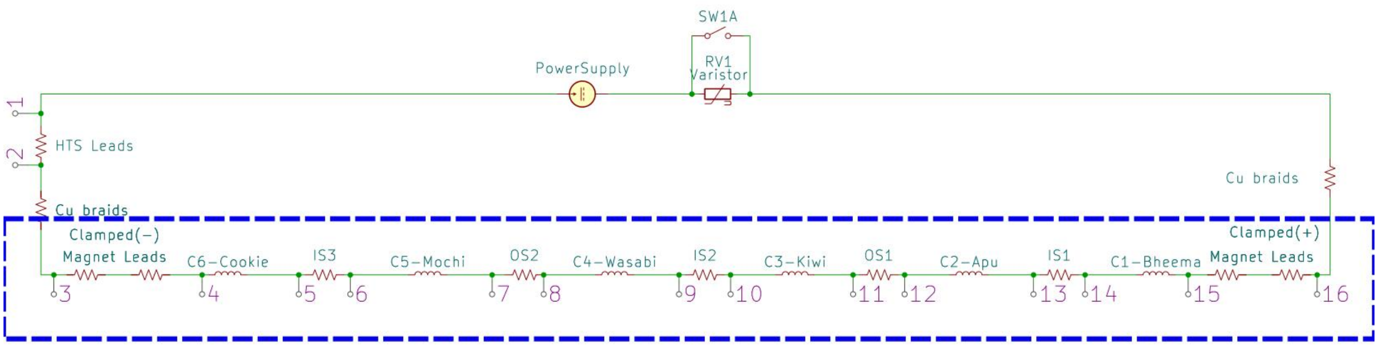

Fig. 15: Instrumentation schematic showing voltage measurement tap locations along the circuit within the cryostat, including connections for individual coils (C1-C6), inner splices (IS1-IS3), outer splices (OS1-OS2), and HTS leads configuration. The dashed-box represents the magnet.

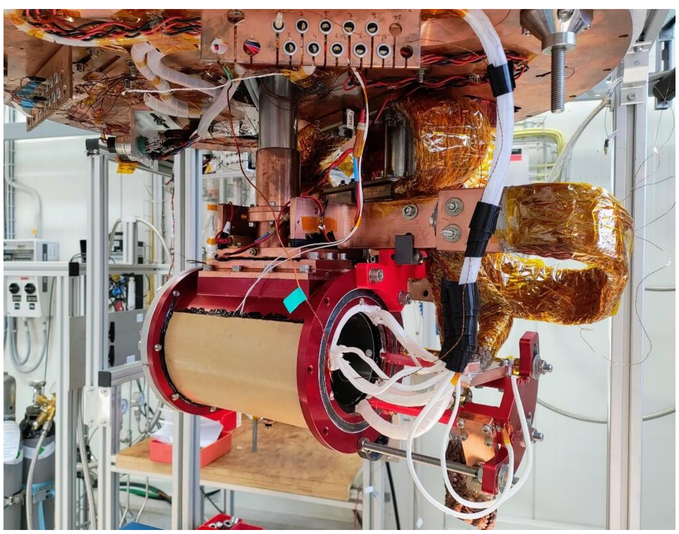

(a) The demonstrator magnet mounted within the cryostat.

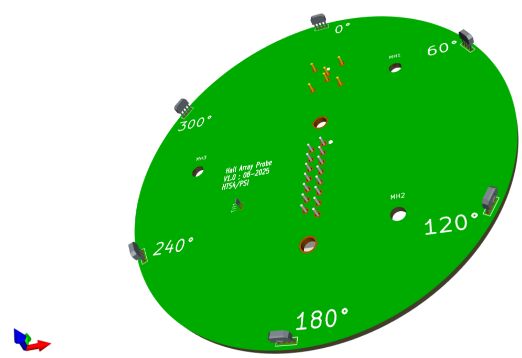

(b) Hall sensor assembly PCB showing the arrangement of magnetic field sensors positioned within the magnet bore.

Fig. 16: Experimental setup showing the HTS4 cos-theta demonstrator magnet mounted within the cryostat, and the Hall sensor PCB used for first-order field characterization during testing operations.

Testing was conducted through systematic current ramping to 370 A, with monitoring of voltage development across individual coils. Figure 17a shows the complete test sequence including ramp-up, plateau hold, and ramp-down phases, and Figure 17b the voltage-current relationship during ramp-up.

Inductance analysis during the ramp-up phase at 1.0 A/s yielded coil inductance contribution of $1.25{\pm}0.07$ mH per coil, resulting in a total magnet inductance of 7.5 mH. Each voltage tap measures the self-inductance of its own coil together with its mutual coupling to the other five, so the six contributions sum to the inductance of the magnet. This measured value can be compared with the two-dimensional simulation of Section II-B, which gives 54.8 mH/m, or 6.0 mH over the 110 mm straight section. The two-dimensional model represents an infinitely long cross-section and therefore excludes the coil ends by construction, so the 1.5 mH difference is attributable to them. Equivalently, the measured inductance corresponds to a magnetic length of 137 mm against a physical straight section of 110 mm: the coil ends hold 195 mm of the 415 mm average turn, that is 47% of the conductor, but contribute only 20% of the inductance.

Splice resistance characterization was performed using linear fits to voltage-current data over the 30–70% current range, revealing inner splice resistances of 150 ± 40 nΩ and outer splice resistances of 230 ± 70 nΩ, with an overall average splice resistance of 180 ± 60 nΩ.

At the 370 A plateau, five coils demonstrated superconducting operation with plateau voltages of 0.07 ± 0.03 mV, which over the 34 m of tape in a coil corresponds to an electric field of at most 0.02 μV/cm, two per cent of the 1 μV/cm critical current criterion.

Individual coil monitoring confirmed the expected perfor-

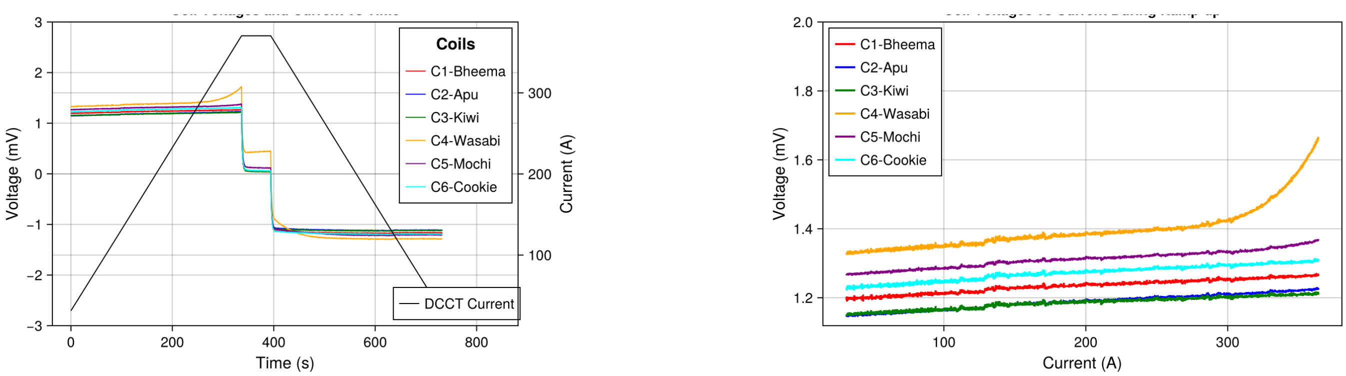

(a) Complete test sequence with current profile during ramp-up (0-340 s), plateau hold at 370 A (340-400 s), and ramp-down (400-740 s) phases.

(b) Voltage-current relationship during ramp-up phase showing linear inductive response for five coils and non-linear behavior in Coil 4 above 270 A.

Fig. 17: Electrical characterization at 40 K showing coil voltage development and current ramping behavior. Coil 4 exhibits consistently higher voltage levels than the other five coils.

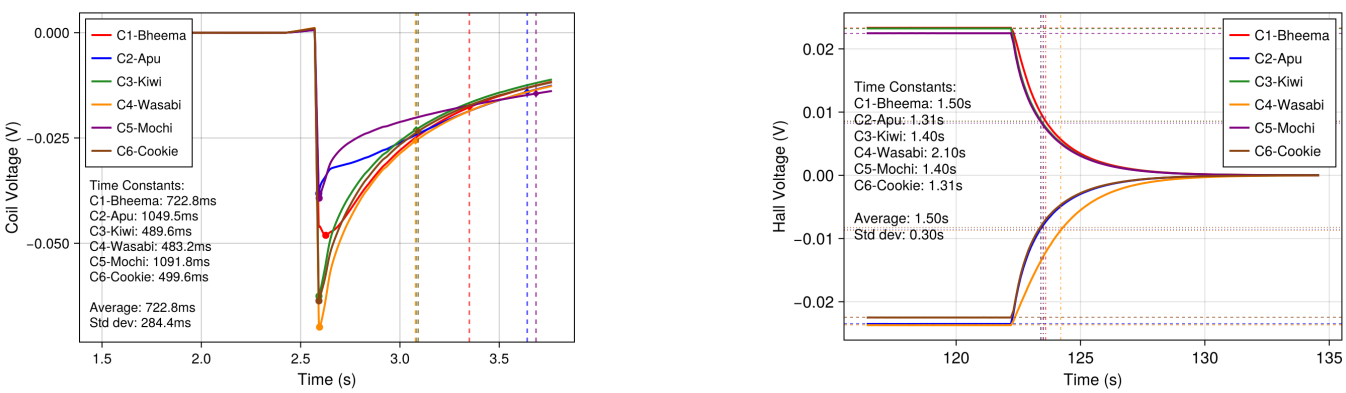

(a) High-resolution voltage-based decay analysis showing time constants of 722 ± 284 ms.

(b) Hall sensor magnetic field decay analysis showing time constants of 1.5 ± 0.3 s.

Fig. 18: Discharge time constant measurements at 40 K using high-resolution voltage measurements across individual coils and Hall sensor magnetic field decay. Results show electromagnetic decay times of 722 ± 284 ms (voltage-based) and 1.5 ± 0.3 s (magnetic field-based).

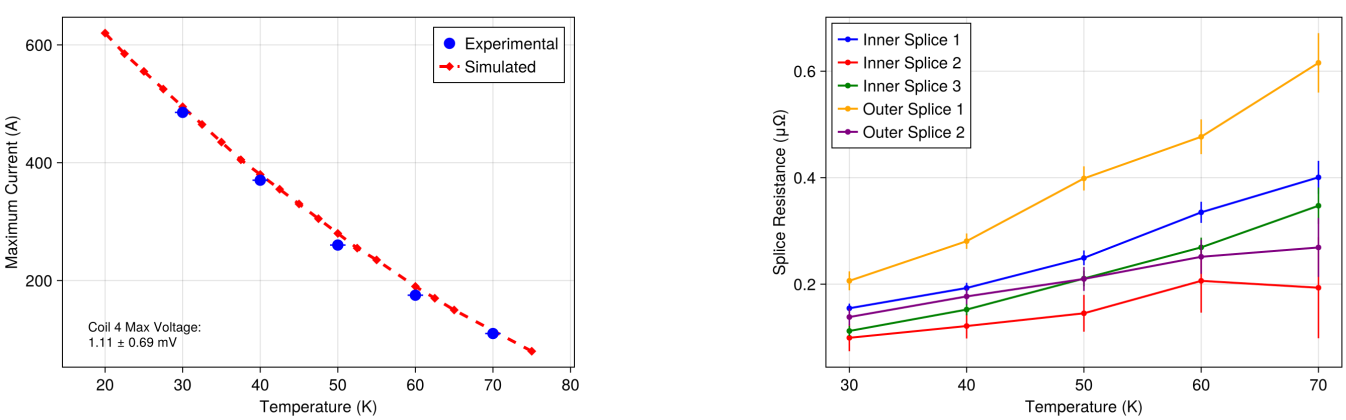

(a) Maximum current vs temperature showing experimental data compared to simulated predictions.

(b) Splice resistance vs temperature for inner splices and outer splices.

Fig. 19: Temperature-dependent performance characteristics showing critical current decreasing from 480 A at 30 K to approximately 100 A at 70 K with excellent agreement to simulated predictions, and splice joint resistance measurements demonstrating stable inter-coil connections with distinct temperature coefficients across the operating temperature range.

mance degradation in Coil 4 due to the scalpel damage sustained during manufacturing (Section IV-B). This damage was identified prior to assembly and had already manifested as under-performance during the preliminary liquid nitrogen tests. As evident in Figure 17a, Coil 4 exhibits consistently higher voltage levels compared to the other five coils throughout the current ramping sequence, and Figure 17b shows a non-linear resistive contribution above approximately 270 A, where the other five coils remain linear. At the 370 A plateau Coil 4 reached 0.45 mV. Averaged over the coil this is an electric field of 0.13 μV/cm, six times that of the other five coils; since the damage is localized, the field at the damaged region is considerably higher.

Hall sensor measurements confirmed proper sextupole field generation, with the alternating polarity across the sensor array reproducing the six-pole symmetry, and a consistent transfer function of 2.49 ± 0.04 mT/A across all sensors. The sensors are located at a radius of 45 mm rather than at the 10 mm reference radius of Table I; since the sextupole field scales as r^2, the measured value corresponds to 0.123 mT/A at 10 mm, or 45.5 mT at 370 A, against the design value of 49.8 mT. The 9% shortfall is comparable to the sensitivity of the measurement to sensor position (a 2 mm error in radius changes the inferred field by 9%) and to the alignment of the sensors with the local field direction. The array therefore confirms the sextupole transfer function to about 10%, but does not resolve the field quality; measurement of the harmonic content would require a rotating coil.

Voltage-based discharge analysis yielded electromagnetic decay times of 722 ± 284 ms (Figure 18a), far longer than the few milliseconds expected from the target contact resistance (Section II-B). These extended time constants indicate lower effective resistance than originally anticipated. With the measured 1.25 mH per coil, a decay time of 722 ms corresponds to an effective resistance of 1.7 mΩ per coil. This implies an apparent average contact resistance of 0.35 mΩ·cm^2: a factor of 286 below the 100 mΩ·cm^2 coating target, and more than three orders of magnitude below the 1020 ± 81 mΩ·cm^2 measured on the coils at room temperature (Section IV-C), which the single-tape measurements[13] indicate should fall by a further factor of 2.5–3 at cryogenic temperature.

Hall sensor measurements within the magnet bore revealed substantially longer magnetic field decay times of 1.5 ± 0.3 s (Figure 18b). This extended decay behavior likely reflects eddy current effects in metallic components of the magnet assembly, e.g., in the aluminum shell, which exhibit longer time constants than the primary superconducting circuit.

C. Critical Current Performance

The critical current performance of the magnet is thus set by the damaged Coil 4, which develops voltage before the other five. The temperature-dependent critical current characterization was performed across the operating range from 30 K to 70 K, with results shown in Figure 19a. The experimental data demonstrates a close agreement with the short sample limit of the tape (Section II-B): the magnet reaches the limit of the conductor itself, and the damage in Coil 4 determines where that limit is detected rather than reducing it. The magnet achieved maximum currents of 480 A at 30 K, decreasing systematically to approximately 100 A at 70 K. At 40 K, the nominal operating temperature, the magnet reached 370 A, equal to the design operating current and confirming the current sharing temperature of 40 K specified in Table II, which by design leaves no current margin there; operation at a lower temperature would restore it. The magnet was also powered up to 470 A at 20 K during the final test described later. Throughout all temperature-dependent characterization, no quench events occurred during controlled current ramping, indicating robust thermal and electromagnetic stability.

The characterization of the splice resistances across the temperature range is shown in Figure 19b. The outer splice 1 exhibited the highest resistance values, ranging from 210 nΩ at 30 K to 630 nΩ at 70 K, while inner splices demonstrated lower and more stable resistance values of 120–400 nΩ across the same temperature range. Inner Splice 2 showed minimal temperature dependence, maintaining approximately 120–200 nΩ throughout the operating range.

The final test had the goal to characterize the quench behavior of the magnet at 20 K. The protection system was not re-enabled for this run, and the (+) magnet current lead burnt out, resulting in an open circuit condition. Post-failure examination revealed no visible macroscopic damage to the lead assembly, suggesting that the failure occurred at the electrical contact between the tapes used to construct the lead. To assess the internal state of the superconducting assembly following the test campaign, the magnet was cross-sectioned for optical examination of the coil structure, partial insulation integrity, and impregnation quality. This ongoing destructive analysis will provide critical data on the robustness of the PVB partial insulation system and wax impregnation methodology under operational thermal and electromagnetic cycling conditions.

VI. Conclusions

The cosine-theta sextupole demonstrator marks a credible way towards REBCO-based short straight sections for FCC-ee. The automated winding, relatively simple mandrel and efficient use of conductor make it a good candidate for large-scale industrial production.

The novel insulation method, in which coils are wound from coated tape and fused into monolithic blocks after winding with a short heat treatment, allows both for a well-controlled turn-to-turn resistance, as well as for easy handling of the coils during installation.

The demonstrator magnet performed at the short sample limit of the HTS tape over a temperature range of 30 K to 70 K, indicating that the cosine-theta geometry is gentle enough on the conductor. Key achievements include reaching the design current of 370 A at the nominal operating temperature of 40 K, a sextupole transfer function confirmed by Hall probes to about 10%, a reproducible room temperature turn-to-turn resistance of 1020 ± 81 mΩ·cm^2 across the six coils, and reproducible manufacturing. The discharge behaviour nevertheless implies a much lower effective contact resistance in operation than either the target or the room temperature value, and this discrepancy remains to be resolved.

The demonstrator did not address topics such as field quality and winding of long-length coils. These will be tackled by the next magnet prototype, a nested cosine-theta type, to be developed by the project. The ongoing destructive analysis of the cross-sectioned demonstrator will inform that design with further data on the partial insulation and impregnation quality.

References

[1] A Abada, M Abbrescia, S S AbdusSalam, I Abdyukhanov, and Abelleira Fernandez. FCC-ee: The Lepton Collider. *The European Physical Journal Special Topics*, 228(2):261–623, 2019. ISSN 1951-6401. doi: 10.1140/epjst/e2019-900045-4. URL https://doi.org/10.1140/epjst/e2019-900045-4.

[2] Jean Paul Burnet. UPDATE OF THE POWER DEMAND ENERGY CONSUMPTION, GRID CONNECTION FOR FCC ee. In *FCC Week 2023*, 2023.

[3] Cristobal Garcia. HTS FCC-ee energy efficient beam optics, 2023.

[4] J. Kosse, M. Koratzinos, and B. Auchmann. Reliability Engineering of Cryocooler-Based HTS Magnets for FCC-Ee. *IEEE Transactions on Applied Superconductivity*, pages 1–5, 2023. ISSN 1051-8223. doi: 10.1109/tasc.2023.3346847. URL https://ieeexplore.ieee.org/document/10373927/.

[5] Mücahid Akbas, Johann W. Kolar, and Jonas Huber. New cryogenic t-type three-switch low-voltage high-current 4q power supply for hts magnets. In *2024 IEEE Energy Conversion Congress and Exposition (ECCE)*, pages 7370–7372, 2024. doi: 10.1109/ECCE55643.2024.10861640.

[6] Thibault Lécrevisse, Xavier Chaud, Philippe Fazilleau, Clément Genot, and Jung-Bin Song. Metal-as-insulation hts coils. *Superconductor Science and Technology*, 35 (7):074004, may 2022. doi: 10.1088/1361-6668/ac49a5. URL https://doi.org/10.1088/1361-6668/ac49a5.

[7] Cristobal Miguel Garcia Jaimes, Adrien Thabuis, Bernhard Auchmann, Jaap Kosse, Léon van Riesen-Haupt, Michael Koratzinos, Mike Seidel, Rogelio Tomas, and Tatiana Pieloni. Parameter space for the magnetic design of Nested Magnets in the FCC-ee arc cell. *JACoW IPAC*, 2024:WEPR11, 2024. doi: 10.18429/JACoW-IPAC2024-WEPR11. URL http://cds.cern.ch/record/2913742.

[8] Stephan Russenschuck. *Field Computation for Accelerator Magnets*. Wiley-VCH Verlag GmbH, 2010. ISBN 0854046356. doi: 10.1002/9783527635467.

[9] Jeroen Van Nugteren and M Danial. Parameterization of the critical surface of REBCO conductors from Bruker, 2017. URL http://cds.cern.ch/record/2277484.

[10] Stuart Wimbush. SuperOx YBCO 2G HTS, 2021.

[11] A. Molodyk, S. Samoilenkov, A. Markelov, P. Degtyarenko, S. Lee, V. Petrykin, M. Gaifullin, A. Mankevich, A. Vavilov, B. Sorbom, J. Cheng, S. Garberg, L. Kesler, Z. Hartwig, S. Gavrilkin, A. Tsvetkov, T. Okada, S. Awaji, D. Abraimov, A. Francis, G. Bradford, D. Larbalestier, C. Senatore, M. Bonura, A. E. Pantoja, S. C. Wimbush, N. M. Strickland, and A. Vasiliev. Development and large volume production of extremely high current density YBa2Cu3O7 superconducting wires for fusion. *Scientific Reports*, 11(1):2084, 2021. ISSN 20452322. doi: 10.1038/s41598-021-81559-z. URL https://www.ncbi.nlm.nih.gov/pubmed/33483553.

[12] Elektrisola. Selfbonding wire types | ELEKTRISOLA. URL https://www.elektrisola.com/en/Products/Selfbonding-Wire/Types#europe.

[13] Matteo Crescenti, Bernhard Auchmann, André Brem, Michał Duda, Jaap Kosse, Colin Müller, Kirtana Puthran, Henrique Rodrigues, Jürgen Schmidt, and Carmine Senatore. Filled thermoplastic based coating for tailored contact resistance in HTS coils. *IEEE Transactions on Applied Superconductivity*, 2025. Under review, EUCAS 2025 Special Issue.